and $D^{2D} = -690 \pm 120$ N m^{-1}, respectively. The intrinsic strength is $\sigma_{int}^{2D} = 42 \pm 4$ N m^{-1}. These correspond to Young's modulus of $E = 1.0 \pm 0.1$ TPa and a third-order elastic stiffness of $D = -2.0 \pm 0.4$ TPa, assuming an effective graphene thickness of 0.335 nm. The corresponding intrinsic stress is $\sigma_{int} = 130 \pm 10$ GPa at a strain of $\varepsilon_{int} = 0.25$. Also, $\sigma_{int} \approx E/8$, which is very close to the value obtained by Griffith.

We compared our measured values with those from other experiments. Experiments on bulk graphite (26) yield 1.02 ± 0.03 TPa for the in-plane Young's modulus. Tensile tests (6–8) have been reported for both single-walled carbon nanotubes and multi-walled carbon nanotubes (MWCNTs). A broad range of stiffness values (0.27 TPa to 1.47 TPa) was obtained, with breaking strengths ranging from 3.6 to 63 GPa and failure strain up to 12%. An in situ tensile test (9) in a TEM reported intrinsic strength of 150 ± 45 GPa for a defect-free MWCNT. At least two recent experiments report mechanical tests performed on suspended graphene films; nanoindentation of suspended multilayer graphene flakes has been used to measure their bending stiffness (12) and extract a Young's modulus of 0.5 TPa (13). The elastic deformation and failure strength of graphene have been simulated using ab initio methods (18, 19). The predicted elastic response is highly nonlinear for strains above 10% and exhibits a maximum for pristine graphite between 118 and 121 GPa.

The intrinsic strength reported here serves as a benchmark for structural and mechanical applications, although the strength of macroscopic graphitic materials is still limited by the presence of defects and grain boundaries. In addition, these measurements demonstrate that third-order elastic constants associated with nonlinear behavior can be measured in atomically perfect nanoscale materials. These measurements can be used to validate models of atomic potentials far beyond the linear regime.

References and Notes
1. A. A. Griffith, *Philos. Trans. R. Soc. London Ser. A* **221**, 163 (1921).
2. Q. Zhao, M. B. Nardelli, J. Bernholc, *Phys. Rev. B* **65**, 144105 (2002).
3. A. Krishnan, E. Dujardin, T. W. Ebbesen, P. N. Yianilos, M. M. J. Treacy, *Phys. Rev. B* **58**, 14013 (1998).
4. J. P. Salvetat et al., *Phys. Rev. Lett.* **82**, 944 (1999).
5. T. W. Tombler et al., *Nature* **405**, 769 (2000).
6. S. Xie, W. Li, Z. Pan, B. Chang, L. Sun, *J. Phys. Chem. Solids* **61**, 1153 (2000).
7. M. F. Yu, B. S. Files, S. Arepalli, R. S. Ruoff, *Phys. Rev. Lett.* **84**, 5552 (2000).
8. M. F. Yu et al., *Science* **287**, 637 (2000).
9. B. G. Demczyk et al., *Mater. Sci. Eng. A* **334**, 173 (2002).
10. B. I. Yakobson, P. Avouris, in *Carbon Nanotubes* (Springer-Verlag, Berlin, 2001), vol. 80, pp. 287–327.
11. K. S. Novoselov et al., *Proc. Natl. Acad. Sci. U.S.A.* **102**, 10451 (2005).
12. M. Poot, H. S. J. v. d. Zant, *Appl. Phys. Lett.* **92**, 063111 (2008).
13. I. W. Frank, D. M. Tanenbaum, A. M. Van der Zande, P. L. McEuen, *J. Vac. Sci. Technol. B* **25**, 2558 (2007).
14. K. S. Novoselov et al., *Proc. Natl. Acad. Sci. U.S.A.* **102**, 10451 (2005).
15. A. C. Ferrari et al., *Phys. Rev. Lett.* **97**, 187401 (2006).
16. Materials and methods are available as supporting material on *Science* Online.
17. R. N. Thurston, K. Brugger, *Phys. Rev.* **133**, A1604 (1964).
18. F. Liu, P. M. Ming, J. Li, *Phys. Rev. B* **76**, 064120 (2007).
19. R. Khare et al., *Phys. Rev. B* **75**, 075412 (2007).
20. R. Al-Jishi, G. Dresselhaus, *Phys. Rev. B* **26**, 4514 (1982).
21. Y. Huang, J. Wu, K. C. Hwang, *Phys. Rev. B* **74**, 245413 (2006).
22. B. I. Yakobson, C. J. Brabec, J. Bernholc, *Phys. Rev. Lett.* **76**, 2511 (1996).
23. J. F. Nye, *Physical Properties of Crystals* (Oxford Univ. Press, New York, 1985).
24. K. T. Wan, S. Guo, D. A. Dillard, *Thin Solid Films* **425**, 150 (2003).
25. U. Komaragiri, M. R. Begley, *J. Appl. Mech.* **72**, 203 (2005).
26. O. L. Blakslee, *J. Appl. Phys.* **41**, 3373 (1970).
27. N. M. Bhatia, W. Nachbar, *Int. J. Non-Linear Mech.* **3**, 307 (1968).
28. B. Lawn, *Fracture of Brittle Solids* (Cambridge Univ. Press, New York, ed. 2, 1993).
29. E. Stolyarova et al., *Proc. Natl. Acad. Sci. U.S.A.* **104**, 9209 (2007).
30. We thank S. Berciaud for Raman spectroscopy of the graphene samples, Namiki Inc. for AFM cantilevers, and J. Hay and W. Oliver (MTS Nano Instruments) for useful interactions. We acknowledge support from NSF under awards CHE-0117752, CMMI-0500239, and DMR-0650555; iMINT (Award HR0011-06-1-0048); Air Force Office of Scientific Research grant FA9550-06-1-0214; and New York State Office of Science, Technology, and Academic Research. This work used shared experimental facilities supported primarily by the Materials Research Science and Engineering Center Program of NSF under award DMR-0213574, and the Cornell Nanoscale Science and Technology Facility, a member of the National Nanotechnology Infrastructure Network, which is supported by NSF (ECS-0335765).

Measurement of the Distribution of Site Enhancements in Surface-Enhanced Raman Scattering

Ying Fang,* Nak-Hyun Seong,* Dana D. Dlott†

On nanotextured noble-metal surfaces, surface-enhanced Raman scattering (SERS) is observed, where Raman scattering is enhanced by a factor, $\overline{G}$, that is frequently about one million, but underlying the factor $\overline{G}$ is a broad distribution of local enhancement factors, η. We have measured this distribution for benzenethiolate molecules on a 330-nanometer silver-coated nanosphere lattice using incident light of wavelength 532 nanometers. A series of laser pulses with increasing electric fields burned away molecules at sites with progressively decreasing electromagnetic enhancement factors. The enhancement distribution $P(\eta)d\eta$ was found to be a power law proportional to $(\eta)^{-1.75}$, with minimum and maximum values of 2.8×10^4 and 4.1×10^{10}, respectively. The hottest sites ($\eta > 10^9$) account for just 63 in 1,000,000 of the total but contribute 24% to the overall SERS intensity.

Molecules on nanotextured noble-metal surfaces (1, 2) or nanoparticle aggregates (3, 4) frequently evidence giant Raman scattering cross sections. This surface-enhanced Raman scattering (SERS) effect has enabled a variety of chemical sensing applications (5), including the detection of single molecules by Raman scattering (6, 7). The average value of the Raman enhancement, $\overline{G}$, is frequently about 10^6 compared with molecules without a SERS substrate. "Hot" spots where the local field enhancement η is 10^9 or more have been detected by searching nanoparticle aggregates with powerful microscopes (6–8). At a hot spot it is possible to measure the Raman spectrum of single molecules (6–8). The existence of hot spots suggests that the average enhancement $\overline{G}$ represents a broad distribution of microscopic enhancement factors, so a SERS signal might result from a few molecules at hot sites or the preponderance of molecules at "cold" sites (9).

SERS mechanisms may involve electromagnetic enhancement, chemical enhancement, or resonance enhancement. The benzenethiolate (BT) molecule is frequently used as a probe of electromagnetic enhancement. BT forms a densely packed, well-ordered self-assembled monolayer (SAM) on Ag (10) of the type frequently used in chemical sensing measurements. Because BT has weak electronic interactions with metal surfaces and does not absorb at the laser wavelength, the chemical and resonance enhancements are unimportant. In electromagnetic enhancement, an incident laser field, E_{in}, excites surface plasmons to create a complex pattern of spatially varying electromagnetic fields (11, 12). At any location, the local field is gE_{in}, where g is the local enhancement factor. For the purposes of this study, it is sufficient to use the approximation (13) that

School of Chemical Sciences, University of Illinois at Urbana-Champaign, Urbana, IL 61801, USA.

*These authors contributed equally to this work.
†To whom correspondence should be addressed. E-mail: dlott@scs.uiuc.edu

the local Raman cross-section enhancement $\eta = \sigma_R^e/\sigma_R^0 = g^4$, where σ_R^e and σ_R^0 are enhanced and unenhanced cross sections, respectively (12). The distribution of local field enhancements will be denoted $P(g)dg$, and the distribution of Raman cross-section enhancements is $P(\eta)d\eta = P(g)dg$.

Electromagnetic calculations have been used to study what sorts of metallic nanostructures create hot sites and how large η could conceivably be at the hottest sites (9, 14–18). One model system for computational studies consists of two closely spaced metal nanoparticles. In the gap between two closely spaced Ag nanoparticles (9, 18–20), η may be as large as 10^{11}. The distribution $P(\eta)d\eta$ has been computed for 25-nm-diameter Ag spheres separated by 2 nm by La Rue and co-workers (9). The computed distribution was a power law proportional to $\eta^{-1.135}$, $\bar{G}$ was 6.7×10^7, and the smallest and largest enhancements were about 1.5×10^3 and 2×10^{10}, respectively.
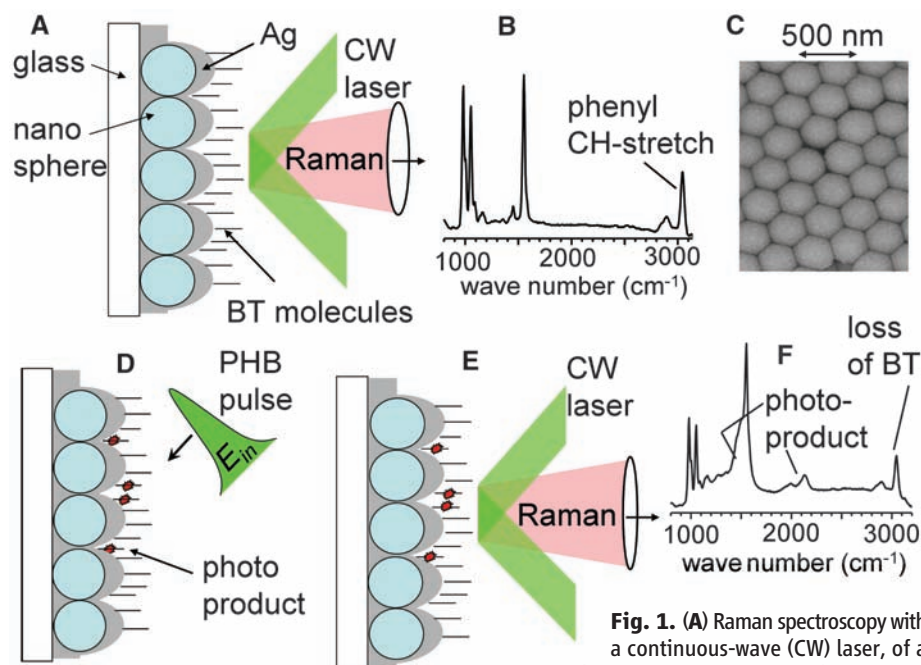
A method to measure $P(\eta)d\eta$ could have several applications. Ordinary Raman measurements are sensitive only to $\bar{G}$, which can lead to difficulties in quantifying SERS signals in analytical applications (21, 22). A great deal of effort has gone into developing methods to fabricate useful SERS materials (23), and a knowledge of $P(\eta)d\eta$ would be more useful than a measurement of $\bar{G}$ to optimize a fabrication technology (22). However, it is not possible to determine $P(g)dg$ or $P(\eta)d\eta$ distributions by using linear Raman ensemble measurements. This task requires either a nonlinear spectroscopy or a molecule-by-molecule census. But single-molecule measurements would not be sensitive enough to observe the colder sites. In studies of molecules in disordered media, photochemical hole burning (PHB), a nonlinear method that involves a burning pulse and a probing pulse (24), has been an effective method for extracting distributions of molecular energy level spacings (25), so an analogous method might be used to measure $P(\eta)d\eta$. Photobleaching of adsorbed dye molecules (9, 26) has been suggested as a method of determining $P(\eta)d\eta$ because the photobleaching efficiency increases in regions of greater local field enhancement. Vibrational pumping of adsorbed dyes has also been suggested in this context (27).

Our method for determining $P(\eta)d\eta$ uses the electric fields from powerful nonresonant laser pulses to photochemically damage molecules adsorbed on a SERS substrate. This type of photodamage is characterized by a sharp electric field threshold, E_{th}. The value of E_{th} depends on the type of molecule, the wavelength, and the pulse duration, but it is typically 1 to 10 GV m^{-1} (28). This sharp threshold behavior, which photobleaching does not exhibit, greatly simplifies the theoretical analysis needed to extract $P(\eta)d\eta$ from experiment. For a given E_{in}, photodamage will occur only at sites where $gE_{in} \geq E_{th}$, so as the PHB laser field is increased molecules with the largest g burn away first, followed by molecules at sites with progressively smaller g. Meanwhile, the sample loses Raman intensity at a rate proportional to $\eta = g^4$ (26). The disappearance of the photodamaged molecules and the appearance of
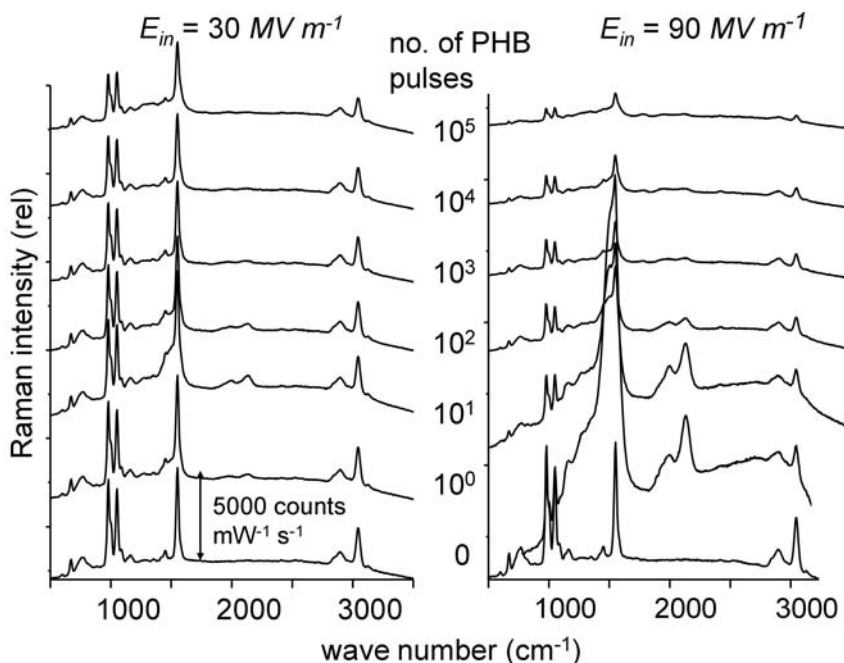
photoproducts can be monitored via Raman spectroscopy with a weak probe laser. In this study, the PHB method is illustrated by using a SERS substrate composed of an Ag film on nanospheres (AgFON) (3–5, 23, 29) having an adsorbed layer of BT.

The experimental concept is depicted in Fig. 1 (30). A BT SAM was deposited on AgFON (330-nm

nanospheres coated by 150-nm Ag) fabricated with use of methods developed by the van Duyne group (23, 29). The 1-ps duration, 532-nm PHB laser pulses were focused to 140 μm (Gaussian $1/e^2$ diameter) spots. The pulse energies ranged from 1 to 1000 nJ, and E_{in} ranged from 10 to 300 MV m^{-1}. A 0.5-mW continuous-wave 532 Raman laser
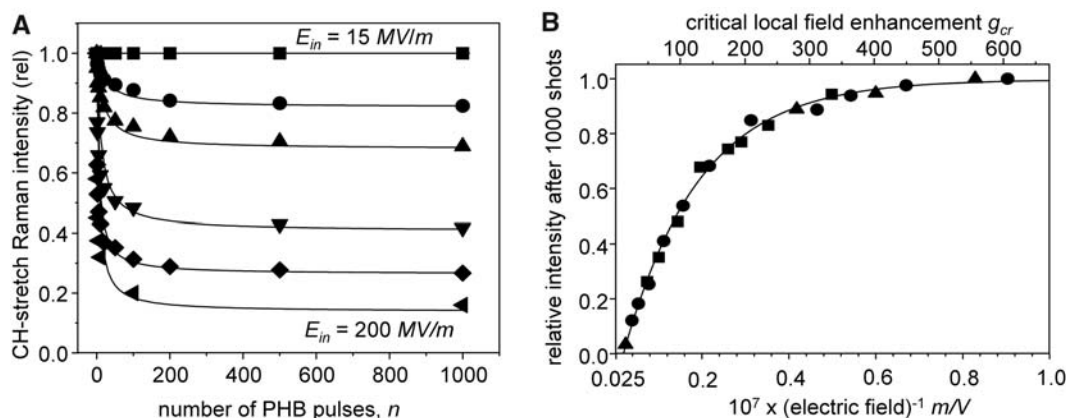

Fig. 1. (**A**) Raman spectroscopy with a continuous-wave (CW) laser, of a SERS sample consisting of AgFON with BT monolayer. (**B**) SERS spectrum of BT. (**C**) Scanning electron micrograph of AgFON surface. (**D**) The sample was exposed to an intense PHB pulse with laser field E_{in}. BT molecules at sites with local field enhancement g were damaged if $gE_{in} \geq E_{th}$, where E_{th} is the threshold field needed to damage BT. (**E** and **F**) The Raman spectrum after PHB shows loss of BT plus new transitions from photoproduct molecules. The loss of BT is quantified by using the integrated area of the phenyl CH-stretch transition at 3050 cm^{-1}.
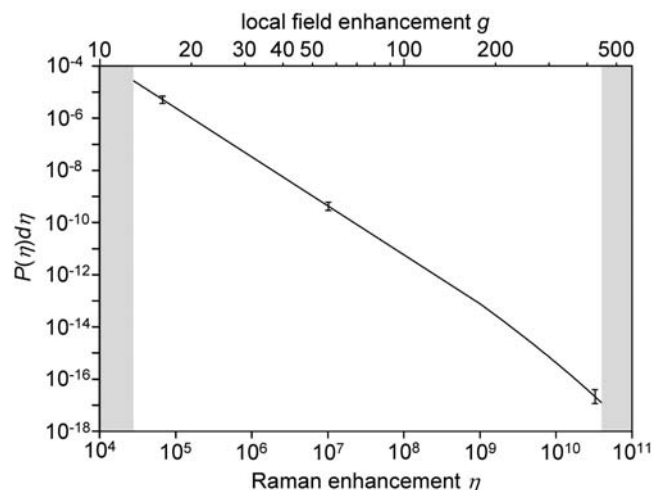

Fig. 2. Raman spectra of BT on an AgFON substrate after the indicated number of PHB pulses, at a lower and higher value of the incident field, E_{in}.

Fig. 3. (**A**) PHB curves for CH-stretch transition of BT molecules on AgFON SERS substrates. From top to bottom, E_{in} = 15, 30, 43, 88, 140, and 200 MV m^{-1}. The smooth curves are calculated from the local field enhancement distribution $P(g)dg$ using the statistical model for PHB of Eq. 1. rel. indicates relative. (**B**) Fraction of BT CH-stretch SERS intensity after 1000 PHB pulses. The different symbols represent measurements on different samples. The PHB curve fits an exponential function (solid line). At given E_{in}, only molecules where the local field enhancement exceeds a critical value g_{cr} (upper abscissa) are damaged by PHB pulses. One-half of the overall SERS signal comes from sites with $g > 100$.

Fig. 4. Measured distribution of SERS enhancement factors $P(\eta)d\eta$ at 532 nm for BT monolayer on AgFON substrate with 330-nm-diameter spheres. The error bars represent estimated errors due to uncertainty in the determination of the ensemble-averaged SERS enhancement $\overline{G}$. Shaded regions denote $\eta_{min} = 2.8 \times 10^4$ and $\eta_{max} = 4.1 \times 10^{10}$.

probed molecules at the center of the PHB beam where E_{in} was spatially uniform to alleviate complications caused by averaging over the spatial beam profile (*26*).

Representative Raman spectra of BT on AgFON after exposure to PHB pulses are shown in Fig. 2. Before PHB the observed spectra agree well with the literature, and the largest peaks give the expected Raman intensity of ~5000 counts mW^{-1} s^{-1} (*3*). The bulk Raman enhancement factor $\overline{G}$ was determined by using the established method (*31*) of comparing the BT SERS intensity to a thin layer of liquid benzenethiol. We used a geometric model for the Ag surface, where the area is a factor $S_{Ag} = 2\pi(R + h)/\sqrt{3R}$ greater than a flat surface (R is the nanosphere radius and h the Ag coating thickness) and the measured value of 3.3×10^{14} cm^{-2} for the molecular packing density on flat Ag(111) (*10*), to obtain $\overline{G} = 8.5 \times 10^5$. Given the possibility of error in our geometric model and the packing density, we assigned a wide error bound of ~50% so that $\overline{G} = 9 \times 10^5 \pm 4 \times 10^5$.

As shown in Fig. 2, in the range of 10 to 100 PHB pulses the BT Raman transitions lose intensity, and new photoproduct transitions grow in, most prominently on the red edge of the 1550

cm^{-1} CH bend and in the 2000 to 2200 cm^{-1} range of carbonyl stretching. On the basis of studies in an O$_2$-depleted atmosphere, we believe that the observed photoproduct results from field ionization of BT to produce a transient species that later reacts with ambient O$_2$. Raman signals from the photoproduct have about the same SERS enhancements as BT. The dramatic spectrum observed after a single PHB pulse at $E_{in} = 9 \times 10^7$ V m^{-1} indicates large SERS enhancement of the photoproduct. This result is compelling evidence that PHB pulses damage BT but not the SERS substrate. As support for this conclusion, we observed that after 10^3 intense PHB pulses with $E_{in} = 200$ MV m^{-1} there was no evident effect on the AgFON surface plasmon resonance.

As the PHB pulse irradiation continued, after 10^3 to 10^4 pulses the photoproduct transitions disappeared. This continued photodamage of the photoproduct further emphasizes that photoproduct molecules reside in local environments that continue to possess large local field enhancements. In the 10^3 to 10^5 pulse regime, BT molecules that were not photodamaged continued to evidence the same Raman spectrum as unirradiated molecules. With subsequent irradiation, after 10^5 to 10^6 high-field pulses, the BT Raman

spectral lineshapes evolved and broadened. We believe that this spectral evolution is associated with gradual laser substrate damage.

To quantify the extent of photodamage, we focused on BT transitions well separated from the photoproduct, specifically the integrated area of the 3050 cm^{-1} peak arising from aromatic CH-stretch transitions. The aromatic phenyl moiety of BT is most susceptible to high-field damage, and nonaromatic photoproducts will have their CH-stretch transitions shifted to the 2850 to 2950 cm^{-1} range. Figure 3A shows a series of burning curves based on monitoring the 3050 cm^{-1} CH stretch. The burning curves were not appreciably different when other BT Raman transitions were monitored. The experimental observable in Fig. 3A is the fractional change $I(n)/I_0$ in Raman intensity after n PHB shots at field E_{in}. Although $I(n)$ is quite dependent on n during the first 100 pulses, the intensity drop caused by photodamage is complete at 1000 pulses. To model this behavior, we assumed that each PHB pulse had a constant probability for inducing photodamage. Then, at a site with enhancement factor g irradiated by n pulses at field E_{in}, this probability $P_{PHB}(g;E_{in},n)$ is

$$P_{PHB}(n;g,E_{in}) = 0, \quad gE_{in} < E_{th}$$
$$P_{PHB}(n;g,E_{in}) = 1 - \exp[-n/n_0], \quad gE_{in} \geq E_{th}$$

(1)

where n_0 is the number of pulses needed to damage $1/e$ of the BT molecules. Then $I(n)/I_0$ can be written in terms of the microscopic distribution function $P(g)dg$

$$\frac{I(n)}{I_0} = \frac{\int_{g_{min}}^{g_{max}} P(g)g^4[1 - P_{PHB}(n; g, E_{in})]dg}{\int_{g_{min}}^{g_{max}} P(g)g^4 dg}$$

$$= \frac{\int_{g_{min}}^{g_{max}} P(g)g^4[1 - P_{PHB}(n; g, E_{in})]dg}{\overline{G}}$$

(2)

Table 1. Contribution of the various site enhancements at 532 nm to the overall SERS signal.

Raman enhancement factor η	Percentage of molecules	Percentage contribution to overall SERS signal
$<2.8 \times 10^4$	0	0
2.8×10^4 to 1×10^5	61%	4%
10^5 to 10^6	33%	11%
10^6 to 10^7	5.1%	16%
10^7 to 10^8	0.7%	22%
10^8 to 10^9	0.08%	23%
10^9 to 10^{10}	0.006%	17%
$>10^{10}$	0.0003%	7%

Although it is possible to determine $P(g)dg$ from the data in Fig. 3A, a more accurate determination was made by averaging the results from five fresh regions of the SERS sample, each exposed to 1000 PHB pulses. We can define a critical value of the local field enhancement $g_{cr} = E_{th}/E_{in}$ such that the probability of photodamage is unity at sites with $g \geq g_{cr}$ and zero at sites with $g < g_{cr}$. Then Eq. 2 becomes

$$\frac{I}{I_0} = \frac{\int_{g_{min}}^{g_{cr}} P(g)g^4 dg}{\overline{G}} = \frac{\int_{\eta_{min}}^{\eta_{cr}} \eta P(\eta) d\eta}{\overline{G}} \quad (3)$$

Equation 3 shows that I/I_0 is a function of $g_{cr} \propto 1/E_{in}$, so in Fig. 3B we plotted I/I_0 versus $1/E_{in}$. To determine $P(g)dg$ from Fig. 3B, we could take the numerical derivative of the data and divide by g^4. However the data in Fig. 3B were unexpectedly well fit by an exponential function, leading to an empirical analytical form for $P(g)dg$ and $P(\eta)d\eta$,

$$P(\eta)d\eta = \frac{A}{\eta^{1.75}} \exp\left(\frac{-\eta^{0.25}}{A'}\right) \quad (4)$$

The value of the constant A in Eq. 4 is determined by the constraint $\int P(g)g^4 dg = \overline{G} = 9 \times 10^5 \pm 4 \times 10^5$. The value of the constant A′ in Eq. 4 is determined by varying the value of E_{th} subject to the normalization condition $\int P(\eta)d\eta = 1$; the best fit was obtained with $E_{th} = 6.7 \pm 0.6$ GV m^{-1}. Knowing E_{th} for BT, with the relation $E_{in}g_{cr} = E_{th}$, we obtain the useful upper abscissa in Fig. 3B. Lastly, we can fit the burning curves in Fig. 3A by using Eqs. 1 and 2 with one additional parameter $n_0 = 10$, which characterizes the number of PHB pulses needed to complete the photodamage process.

In order to properly normalize $P(\eta)d\eta$, we need to know the minimum and maximum enhancement values, η_{max} and η_{min}. To determine η_{max}, we need to determine the weakest pulse that causes the first detectable photodamage. From Fig. 3B, this E_{in} value corresponds to $g_{cr} = 450$ or $\eta_{max} = 4.1 \times 10^{10}$. To determine η_{min}, we need to determine the weakest E_{in} that photodamages every molecule on the surface. Unfortunately, we could not do this without damaging the SERS substrate, so we could not extend Fig. 3A below $g_{cr} = 20$ and $\eta_{min} = 1.6 \times 10^5$. It seems reasonable to extrapolate the exponential in Fig. 3B to where it intersects the abscissa at $g_{cr} = 13$ and $\eta_{min} =$

2.8×10^4. The resulting $P(\eta)d\eta$ at 532 nm is shown in Fig. 4. The distribution of site enhancements is a power law with $\eta^{-1.75}$ dependence, but at the largest enhancements, $\eta > 10^9$, the distribution drops off even more steeply. Thus, our measured distribution for a periodic lattice of 330-nm adjacent nanospheres falls off faster than the $\eta^{-1.135}$ dependence obtained theoretically by La Rue and co-workers (9). The La Rue calculation (9) refers to a pair of 25-nm spheres separated by 2 nm rather than a lattice of spheres, but interestingly the authors speculated that for a collection of spheres the main difference would be a faster drop off at large η such as we see in Fig. 4. The fraction of molecules at each enhancement and the contributions of the different site enhancement factors η to the overall SERS signal are given in Table 1, derived by using Fig. 3B and numerical integration of Fig. 4. The distribution we present applies to AgFON substrates with the specific geometry used here and might be quite different for other SERS materials.

This study used 1-ps, 532-nm PHB pulses, but we know no reason why other PHB pulse durations and wavelengths could not be used. Ultrashort pulses may not be required but are desirable because at a given E_{in} ultrashort pulses pose less risk of substrate damage. We believe that the largest source of experimental error is our error in determining $\overline{G}$. The resulting uncertainty in $P(\eta)d\eta$ is illustrated by the error bars in Fig. 4. Our measured distribution terminates at $\eta_{max} = 4.1 \times 10^{10}$. There may be a small number of hotter sites, but they represent such a tiny fraction of the overall SERS intensity that if they existed we could not detect them. The value $\eta_{min} = 2.8 \times 10^4$ is based on extrapolation, and if there were more or fewer cold sites than the extrapolation indicates, the fraction of hot sites in Table 1 would become proportionately smaller or larger.

Table 1 answers many questions about the inhomogeneous nature of the AgFON SERS substrate. The coldest sites ($\eta < 10^5$) contain 61% of the molecules but contribute just 4% of the overall SERS intensity. The hottest sites ($\eta > 10^9$) comprise just 63 molecules per million but contribute 24% of the overall SERS intensity.

Our PHB technique should be capable of measuring distributions on other SERS materials provided these substrates can withstand PHB pulses. A particularly interesting system involves stripping away the Ag-coated nanospheres (23, 31),

leaving behind a periodic array of nanotriangles. The reduced area of the nanotriangle substrate, about 3% of the AgFON surface area for BT binding, reduces the overall SERS intensity but increases the average enhancement $\overline{G}$ of the remaining surface. If we assume the stripping process removes the coldest 97% of the BT molecules, then from the $P(\eta)d\eta$ distribution found here we would predict the average enhancement for BT on nanotriangles to be $\overline{G} = 2 \times 10^7$, about 20 times greater than for AgFON. Although we cannot directly compare the nanotriangle experiments to the present work because the Ag thickness, sphere diameters, and wavelengths were slightly different, with a substrate that performed optimally at 625-nm laser wavelength McFarland et al. (31) obtained $\overline{G} = 1.2 \times 10^7$ and with a 670-nm substrate $\overline{G} = 1.4 \times 10^7$.

References and Notes

1. M. Fleischmann, P. J. Hendra, A. J. McQuillan, Chem. Phys. Lett. **26**, 163 (1974).
2. D. L. Jeanmaire, R. P. Van Duyne, J. Electroanal. Chem. **84**, 1 (1977).
3. C. L. Haynes, R. P. Van Duyne, J. Phys. Chem. B **105**, 5599 (2001).
4. K. A. Willets, R. P. Van Duyne, Annu. Rev. Phys. Chem. **58**, 267 (2007).
5. C. R. Yonzon, X. Y. Zhang, J. Zhao, R. P. Van Duyne, Spectroscopy **22**, 42 (2007).
6. K. Kneipp, H. Kneipp, I. Itzkan, R. R. Dasari, M. S. Feld, Chem. Phys. **247**, 155 (1999).
7. J. T. Krug II, G. D. Wang, S. R. Emory, S. Nie, J. Am. Chem. Soc. **121**, 9208 (1999).
8. J. A. Dieringer, R. B. Lettan, K. A. Scheidt, R. P. van Duyne, J. Am. Chem. Soc. **129**, 16249 (2007).
9. E. C. Le Ru, P. G. Etchegoin, M. Meyer, J. Chem. Phys. **125**, 204701 (2006).
10. J. Y. Gui et al., Langmuir **7**, 955 (1991).
11. M. I. Stockman, Phys. Rev. E **56**, 6496 (1997).
12. M. Moskovits, in Surface-Enhanced Raman Scattering: Physics and Applications, vol. 103 of Topics in Applied Physics, K. Kneipp, M. Moskovits, H. Kneipp, Eds. (Springer-Verlag, Berlin, 2006), pp. 10–18.
13. E. C. Le Ru, P. G. Etchegoin, Chem. Phys. Lett. **423**, 63 (2006).
14. P. K. Aravind, H. Metiu, J. Phys. Chem. **86**, 5076 (1982).
15. P. K. Aravind, H. Metiu, Surf. Sci. **124**, 506 (1983).
16. P. K. Aravind, A. Nitzan, H. Metiu, Surf. Sci. **110**, 189 (1981).
17. N. Liver, A. Nitzan, J. I. Gersten, Chem. Phys. Lett. **111**, 449 (1984).
18. G. C. Schatz, M. A. Young, R. P. van Duyne, in Surface-Enhanced Raman Scattering: Physics and Applications, vol. 103 of Topics in Applied Physics, K. Kneipp, M. Moskovits, H. Kneipp, Eds. (Springer-Verlag, Berlin, 2006), pp. 19–46.
19. H. X. Xu, J. Aizpurua, M. Käll, Phys. Rev. E **62**, 4318 (2000).
20. H. X. Xu, M. Käll, ChemPhysChem **4**, 1001 (2003).
21. E. C. Le Ru, E. Blackie, M. Meyer, P. G. Etchegoin, J. Phys. Chem. C **111**, 13794 (2007).
22. M. Natan, Faraday Discuss. **132**, 321 (2006).
23. X. Y. Zhang, A. V. Whitney, J. Zhao, E. M. Hicks, R. P. Van Duyne, J. Nanosci. Nanotech. **6**, 1920 (2006).
24. S. Mukamel, Principles of Nonlinear Optical Spectroscopy (Oxford Univ. Press, New York, 1995).
25. W. W. Parson, Modern Optical Spectroscopy (Springer, Berlin, 2007).
26. B. Pettinger, B. Ren, G. Picardi, R. Schuster, G. Ertl, J. Raman Spectrosc. **36**, 541 (2005).
27. P. G. Etchegoin, E. C. Le Ru, R. C. Maher, L. F. Cohen, Phys. Chem. Chem. Phys. **9**, 4923 (2007).
28. K. Toyota, S. Nakashima, T. Okada, Chem. Phys. Lett. **323**, 323 (2000).
29. X. Zhang, M. S. Young, M. A. Lyandres, R. P. Van Duyne, J. Am. Chem. Soc. **127**, 4484 (2005).

30. Materials and methods are detailed in supporting online material available at *Science* Online.
31. A. D. McFarland, M. A. Young, J. A. Dieringer, R. P. van Duyne, *J. Phys. Chem. B* **109**, 11279 (2005).
32. This material is based on work supported by NSF under award DMR 0504038, the Air Force Office of Scientific Research under award FA9550-06-1-0235, and the Army Research Office under award W911NF-05-1-0345. Electron microscopy

Patagonian Glacier Response During the Late Glacial–Holocene Transition

Robert P. Ackert Jr.,[1]* Richard A. Becker,[2] Brad S. Singer,[2] Mark D. Kurz,[3] Marc W. Caffee,[4] David M. Mickelson[2]

Whether cooling occurred in the Southern Hemisphere during the Younger Dryas (YD) is key to understanding mechanisms of millennial climate change. Although Southern Hemisphere records do not reveal a distinct climate reversal during the late glacial period, many mountain glaciers readvanced. We show that the Puerto Bandera moraine (50°S), which records a readvance of the Southern Patagonian Icefield (SPI), formed at, or shortly after, the end of the YD. The exposure age (10.8 ± 0.5 thousand years ago) is contemporaneous with the highest shoreline of Lago Cardiel (49°S), which records peak precipitation east of the Andes since 13 thousand years ago. Absent similar moraines west of the Andes, these data indicate an SPI response to increased amounts of easterly-sourced precipitation—reflecting changes in the Southern Westerly circulation—rather than regional cooling.

First detected in pollen records from northern Europe, the Younger Dryas (YD) chronozone is perhaps best expressed in Greenland ice cores (*1*) that show an abrupt return to near-glacial conditions in the North Atlantic region during the last deglaciation between 12.9 and 11.6 thousand years ago (ka). Less extreme, but extensive, cooling occurred throughout the Northern Hemisphere (*2*). Comparison of temperature records from Greenland and Antarctic ice cores during the last deglaciation indicate antiphased behavior, however (*3*); the Antarctic Cold Reversal (ACR) preceded the YD interval and Antarctic warming occurred during the YD, peaking at ~11 ka. Determining whether the Southern Hemisphere mid-latitudes follow a North Atlantic or an Antarctic signal remains key to deciphering the mechanisms responsible for millennial and abrupt climate change (*4*).

In general, climate records from New Zealand and Patagonia lack evidence of a distinct climate reversal during the late glacial period [see the supporting online material (SOM) text]. Yet there

is clear evidence for prominent glacial readvances in both New Zealand's Southern Alps (*5*, *6*) and the Southern Andes after ~15 ka (*7*). In New Zealand, the Waiho Loop moraine, which was previously inferred to be of YD age on the basis of ^{14}C ages of reworked wood, may be significantly younger in accordance with cosmogenic surface-exposure ages of moraine boulders (*8*, *9*). ^{14}C ages provide only broadly limiting constraints on late glacial advances in Patagonia. Thus, both the timing and synchrony of Southern Hemisphere glacial readvances remain poorly constrained.

The Puerto Bandera moraines at Lago Argentino, Argentina (50°S), consist of two terminal moraine belts (PB I and PB II) that can be distinguished on the basis of field observations and interpretation of remote imagery (*10*). The moraines occur along both the northern and southern shore of the lake with the younger (PB II) moraine crosscutting the older (PB I) near the present shoreline (Fig. 1C). Lying within the Patagonian steppe, where precipitation is currently only ~200 mm/year, the moraines record readvances of Southern Patagonian Icefield (SPI) outlet glaciers that extended 40 km beyond the nearest present-day ice margins.

Three ^{14}C dates of peat overlying gravel from an abandoned outlet channel in the nearby Brazo Rico moraine (Fig. 1C) with a weighted mean age of 11.7 ± 0.3 ka (*10–12*) have been taken as a minimum age of the Puerto Bandera moraines (*13*). Although the ages are consistent with a YD age for the Brazo Rico moraine, Mercer considered this interpretation unlikely because

it requires a very rapid retreat of the ice front at the end of the YD (*11*); peat could not begin to accumulate in the outlet channel until the glacier had retreated to the position of the present Perito Moreno Glacier, thereby opening a lower outlet to Lago Argentino along its terminus (Fig. 1C). Strelin and Malagnino report ^{14}C ages of reworked peat in lateral moraines in Brazo Norte (Fig. 1C) (*10*). An age of 15.5 ± 2.4 ka was obtained from a PB I moraine and an age of 12.9 ± 2.1 ka was obtained from a PB II moraine. The ^{14}C ages of reworked peat show that the SPI had retreated within the Cordillera at these times and indicate that the terminal Puerto Bandera moraines record a large-scale readvance of the SPI.

To better constrain the age of the Puerto Bandera moraines and to evaluate Southern Hemisphere climate during the YD interval, we determined the exposure ages of 18 moraine boulders using cosmogenic ^{36}Cl and ^{10}Be. Samples were collected from the outermost moraine crests on both the northern and southern side of the lake. Fifteen samples are from PB I and three samples are from PB II (Fig. 1C). Boulders were selected on the basis of size, shape, quartz content (for the ^{10}Be samples), and lack of weathering in order to reduce geologic uncertainties. The ^{36}Cl and ^{10}Be production rates have been scaled for elevation, latitude, and atmospheric pressure (*14*). Adjustments for erosion and secular variation of the magnetic field were unnecessary. We estimate that uncertainties in our exposure ages, including scaling factors, are ~6% (*15*).

The arithmetic means of the ^{10}Be and ^{36}Cl exposure ages are 10.8 ± 2.1 ka and 10.8 ± 2.9 ka, respectively (Table 1). More involved statistical treatment relies on the assumption that the exposure ages comprise a normal distribution, specifically, that all samples have an identical simple exposure history and that scatter in the ages results from normally distributed analytical uncertainties. We tested this assumption using a χ^2 analysis. We found the youngest ^{36}Cl and ^{10}Be exposure ages to be outliers based on the low probability that the samples come from a single normal distribution (*16*). The weighted mean of the remaining ^{10}Be ages is 10.8 ± 0.6 ka; that of the remaining ^{36}Cl ages is 10.9 ± 0.9 ka (Table 1 and tables S2 and S3). All 16 samples yielded an inverse-variance weighted mean age of 10.8 ± 0.5 ka (the mean square weighted deviation is 0.80). Given that the scatter in the ages can be attributed mostly to normally distributed analytical errors, we inferred that

[1]Department of Earth and Planetary Science, Harvard University, 20 Oxford Street, Cambridge, MA 02138, USA. [2]Department of Geology and Geophysics, University of Wisconsin–Madison, 1215 West Dayton Street, Madison, WI 53706, USA. [3]Woods Hole Oceanographic Institution, Clark 419, MS #25, Woods Hole, MA 02543, USA. [4]Purdue Rare Isotope Measurement Laboratory, Purdue University, 525 Northwestern Avenue, West Lafayette, IN 47907–2036, USA.

*To whom correspondence should be addressed. E-mail: rackert@fas.harvard.edu